Supporting Information for

MASS TRANSFER LIMITATIONS OF POROUS SILICON-BASED BIOSENSORS FOR PROTEIN DETECTION

*Sofia Arshavsky Graham,[a,b] Evgeniy Boyko,[c] Rachel Salama[a], and Ester Segal [a,d]**

[a] Department of Biotechnology and Food Engineering, Technion – Israel Institute of Technology, Haifa 3200003, Israel

[b] Institute of Technical Chemistry, Leibniz Universität Hannover, Callinstr. 5, 30167 Hanover, Germany

[c] Department of Mechanical Engineering, Technion – Israel Institute of Technology, Haifa, 3200003, Israel

[d] The Russell Berrie Nanotechnology Institute, Technion – Israel Institute of Technology, Haifa 3200003, Israel

* *E-mail: esegal@technion.ac.il*

Table of Contents

Derivation of a Planar Model for the PSi-Based Biosensors (Perfect Collector Assumption)

The PSi biosensor is modeled as a perfect collector, as previously described by Lazzara *et al* [1]. One dimensional diffusion in the z direction is assumed. The analyte of interest is introduced to the PSi biosensor at an initial concentration c_{A0} and diffuses in the bulk solution towards the PSi surface with a diffusivity coefficient D_{bulk}. Bioreceptor molecules are immobilized on the PSi surface at a density of b_m. The change in analyte concentration in bulk solution is described by Fick's second law:

$$\frac{\partial c_{A,bulk}}{\partial t} = D_{bulk}\frac{\partial^2 c_{A,bulk}}{\partial z^2} \quad 0 < z < H \tag{S-1}$$

With the following initial and no-flux boundary conditions:

$$c_{A,bulk}(z, t=0) = c_{A0} \qquad 0 \le z \le H \tag{S-2}$$

$$\frac{\partial c_{A,bulk}}{\partial z} = 0 \quad \text{at} \quad z = 0 \tag{S-3}$$

At the PSi surface, the following boundary condition is applied, assuming continuity between the diffusive flux and reactive flux:

$$\frac{\partial b}{\partial t} = -\frac{d_p}{4L_p} D_{bulk}\frac{\partial C_{A,bulk}}{\partial z} \quad \text{at} \quad z = H \tag{S-4}$$

where b is the bound analyte-bioreceptor complex density on the PSi surface, d_p is the pore diameter and L_p is the porous layer thickness. Since both fluxes relate to a different area,

equation (S-4) considers the area ratio between the pore entry area ($\frac{\pi d_p^2}{4}$) and the total area of the pore for reaction ($\frac{\pi d_p^2}{4} + \pi d_p L_p$), while assuming $d_p = L_p$:

$$\text{Ratio} = \frac{\frac{\pi d_p^2}{4}}{\frac{\pi d_p^2}{4} + \pi d_p L_p} = \frac{\frac{d_p}{4}}{\frac{d_p}{4} + L_p} \overset{\frac{d_p}{4} = L_p}{=} \frac{\frac{d_p}{4}}{\frac{d_p}{4} + L_p} = \frac{d_p}{4L_p}. \quad \text{(S-5)}$$

The change in the bound complex density is described by:

$$\frac{\partial b}{\partial t} = k_{on}(b_m - b)c_{A,bulk}\,|_{z=H} - k_{off} b, \quad \text{(S-6)}$$

with initial condition:

$$b(z = H, t = 0) = 0. \quad \text{(S-7)}$$

Comparison of Theoretical Models to Experimental Results

Table S1. *Fitting parameters used for the numerical simulations, based on the properties of the different aptasensors*

Parameter	Description	Units	Protein A	D2	Tyrosinase	AGR2	Simulation
$\boldsymbol{H}$	Height of solution above PSi	m	0.001	0.001	0.001	0.001	**0.001**
$\mathbf{L_p}$	Porous layer thickness	m	$5.5\cdot10^{-6}$	$5.5\cdot10^{-6}$	$5.5\cdot10^{-6}$	$5.0\cdot10^{-6}$	$\mathbf{5.5\cdot10^{-6}}$
$\mathbf{D_{bulk}}$	Analyte diffusivity in bulk	$\frac{m^2}{s}$	$7\cdot10^{-11}$	$7\cdot10^{-11}$	$7\cdot10^{-11}$	$7\cdot10^{-11}$	$\mathbf{7\cdot10^{-11}}$
$\mathbf{d_{p0}}$	Initial average pore diameter	m	$5\cdot10^{-8}$	$5\cdot10^{-8}$	$5\cdot10^{-8}$	$5\cdot10^{-8}$	$\mathbf{5\cdot10^{-8}}$
$\mathbf{d_A}$	hydrodynamic diameter of analyte	m	$\sim5.3\cdot10^{-9}$	$\sim6\cdot10^{-9}$	$\sim4.0\cdot10^{-9}$	$\sim5.0\cdot10^{-9}$	$\mathbf{\sim5.3\cdot10^{-9}}$
$\mathbf{d_B}$	hydrodynamic diameter of probe	m	$\sim3\cdot10^{-9}$	$\sim3\cdot10^{-9}$	$\sim3\cdot10^{-9}$	$\sim3\cdot10^{-9}$	$\mathbf{\sim3\cdot10^{-9}}$
$\mathbf{k_{on}}$	Reaction association rate	$\frac{1}{M\cdot s}$	$1.21\cdot10^{3}$ [2]	n.a.	n.a.	n.a.	$\mathbf{1.21\cdot10^{3}}$
$\mathbf{k_{off}}$	Reaction dissociation rate	$\frac{1}{s}$	$6.32\cdot10^{-4}$ [2]	n.a.	n.a.	n.a.	$\mathbf{6.32\cdot10^{-4}}$
$\mathbf{K_D}$	Dissociation constant	M	$0.522\cdot10^{-6}$ [2]	$4.6\cdot10^{-6}$	$4.6\cdot10^{-6}$	$0.013\cdot10^{-6}$	**-**

*n.a. – values are not available

Table S2. *Quantification of immobilized aptamer concentration and surface density on the $PSiO_2$*

Aptasensor	$PSiO_2$ volume (cm^3)	$PSiO_2$ surface area (cm^2)	Moles of cleaved aptamer (nmol)	C_{B0} Concentration inside the $PSiO_2$ (mM)	b_m Density inside the $PSiO_2$ (mol m^{-2})
Anti-AGR2	$2.73 \cdot 10^{-4}$	827	0.28±0.05	1.0±0.2	$(3.3 \pm 0.6) \cdot 10^{-9}$
Anti-his tag	$3.01 \cdot 10^{-4}$	910	1.89±0.02	6.28±0.06	$(2.07 \pm 0.02) \cdot 10^{-8}$

The concentration of the aptamer capture probes was experimentally determined for the anti-AGR2 and anti-his tag aptasensors, which slightly differ in the porous nanostructure characteristics, the aptamer concentration utilized for the immobilization, and the surface chemistry protocol (mainly the amino-silanization). Thus, the results give a reliable range for the immobilized aptamers for all studied aptasensors. Immobilized aptamer concentration and surface density are determined by dividing the cleaved aptamer moles from the surface by the total porous volume of area, respectively. The latter was measured in a previous study by nitrogen adsorption isotherms and application of BET (Brunauer-Emmett-Teller) model for a similar $PSiO_2$ nanostructure [3]. Since the $PSiO_2$ utilized in the present study was characterized with a smaller layer thickness (5000-5500 nm vs. 7880 nm), the surface area was corrected according to the layer thickness ratio of both nanostructures. The area of the $PSiO_2$ sample is 1.33 cm^2.

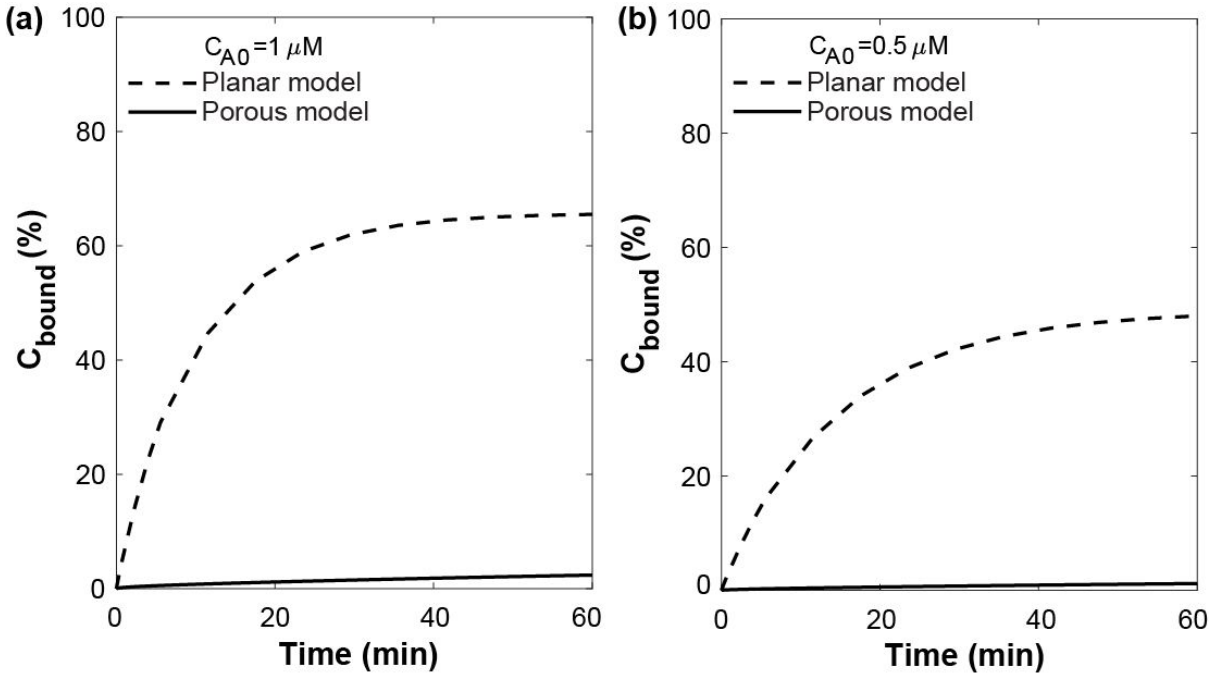

Figure S1. *Simulated binding rates for the porous and planar models at target concentrations of (a) 1 μM and (b) 0.5 μM. The curves present the bound analyte, normalized to the probe concentration, at the bottom of the pore as a function of time.*

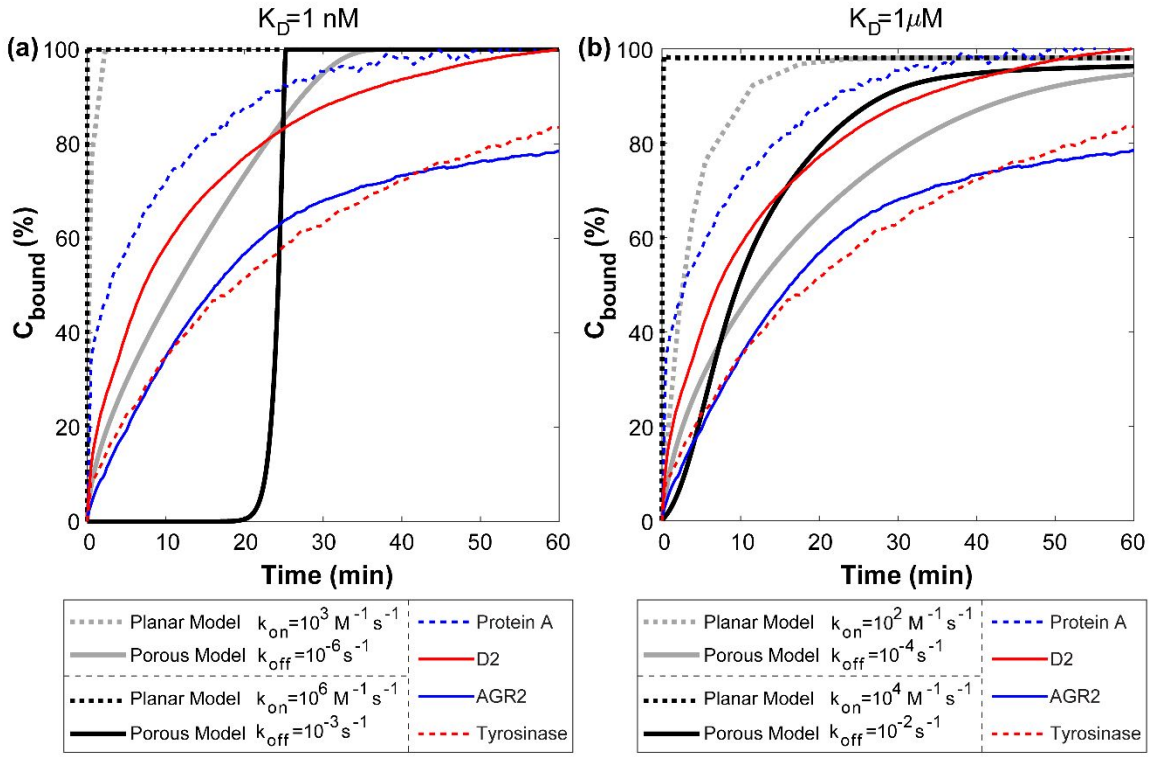

Figure S2. *Comparison of experimental binding curves of the investigated aptasensors, at target concentration of 50 μM to numerical simulation results obtained for the porous and planar models, for two different binding affinity interactions with (a) K_D=1 nM and (b) K_D=1 μM. For the experimental data, the EOT signals for each aptasensor were normalized to the maximal EOT signal obtained upon aptasensor saturation with the target. For the simulated binding, the curves present the bound analyte concentration at the bottom of the pore as a function of time.*

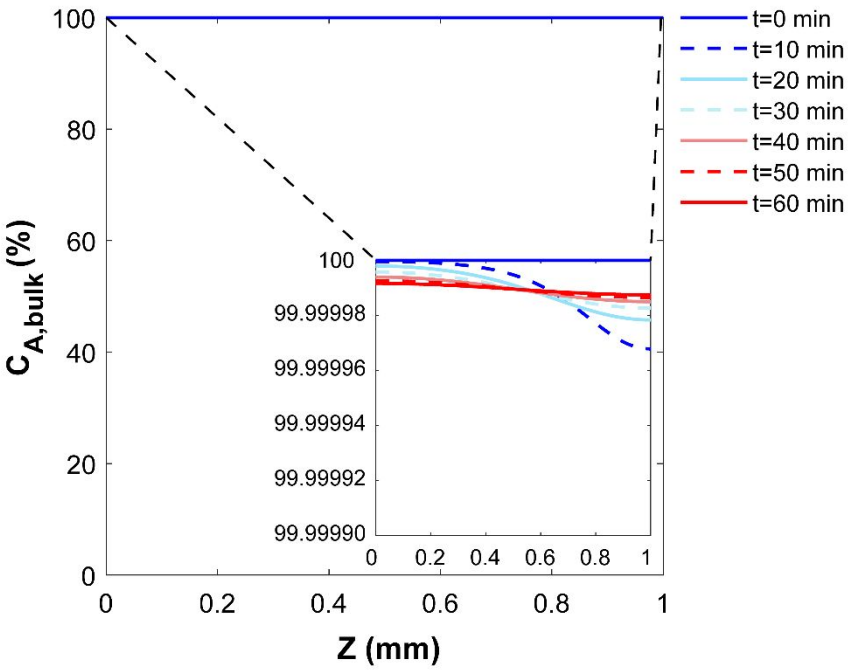

Figure S3. *Change in target concentration in z axis in the bulk solution at different time points, simulated by the planar model. The aptasensor parameters were applied for the simulation and the concentration is normalized to the initial target concentration solution of 50 µM.*

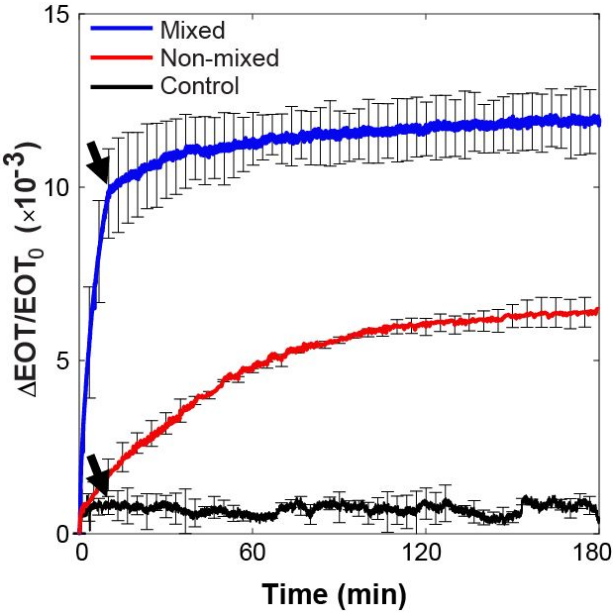

Figure S4. *Relative EOT changes as a function of time for 10 min-mixed and non-mixed AGR2 (11.4 μM) biosensing experiments on anti-AGR2 aptasensor. As a control, the protein dilution buffer is mixed on the aptasensor for 10 min. Black arrows indicate the transfer from mixing to incubation. The results show the significant enhancement in binding rate and total signal obtained upon mixing.*

The Effect of the PSi Porosity on the Binding Rate

The PSi porosity affects the boundary condition requiring a diffusion flux continuity between the bulk solution and the porous layer at the pore entry:

$$A_1 \cdot D_{bulk} \frac{\partial c_{A,bulk}}{\partial z} = A_2 \cdot D_{PSi} \frac{\partial c_{A,PSi,\text{single}}}{\partial z} \quad \text{at} \quad z = H \tag{S-8}$$

where A_1 is the surface area of the cell chamber, given by $A_1 = \frac{\pi d_{cell}^2}{4}$, where d_{cell} is the cell diameter. A_2 is the surface area of the pore entries, given by $A_2 = N_{pores} \cdot \frac{\pi d_p^2}{4}$, where N_{pores} is the number of pores and d_p is the average pore diameter. The ratio of A_2 and A_1 is the porosity of the porous layer, termed P. Thus, the boundary condition is given by

$$D_{bulk} \frac{\partial c_{A,bulk}}{\partial z} = P \cdot D_{PSi} \frac{\partial c_{A,PSi,\text{single}}}{\partial z} \quad \text{at} \quad z = H \tag{S-9}$$

The effect of the porosity (and accordingly the number of pores) is presented in Figure S5, demonstrating higher binding rates for decreasing porosities.

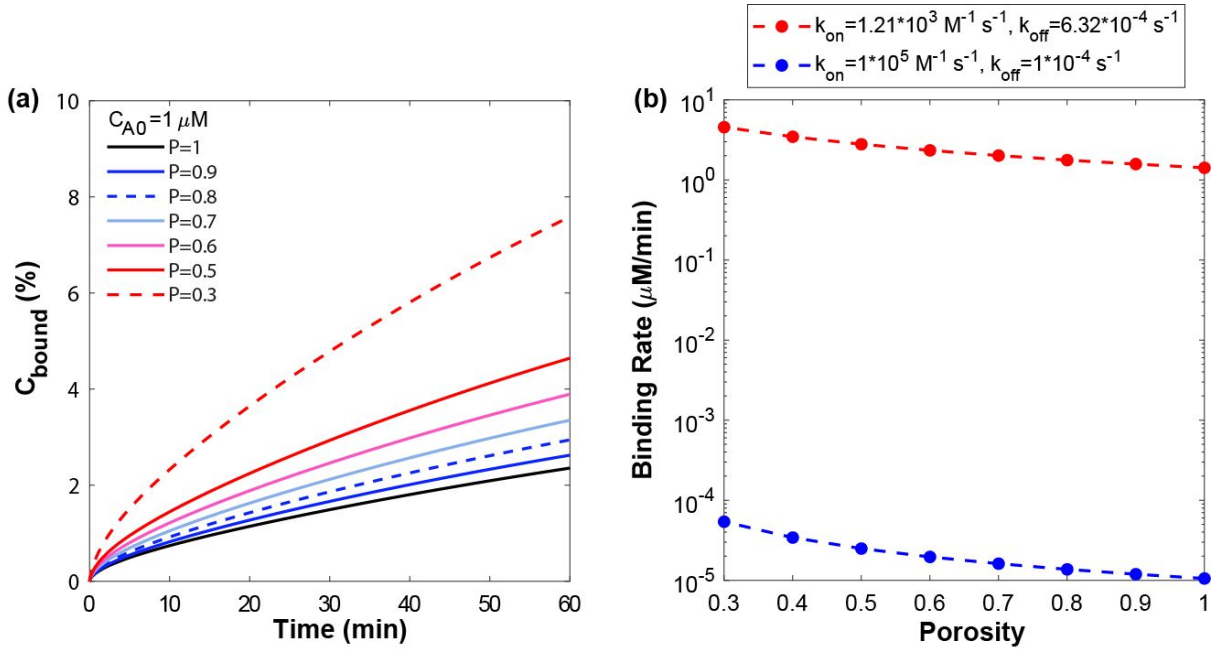

Figure S5. *(a) Simulated binding rate for the porous model, for different PSi porosity values (P), at a target concentration of 1 μM. The curves present the bound analyte, normalized to the probe concentration, at the bottom of the pore as a function of time. (b) Simulated effect of the PSi porosity on the target binding rate for a target concentration of 1 μM, for low (*$k_{on} = 1.21 \cdot 10^3 M^{-1} s^{-1}$ and $k_{off} = 6.32 \cdot 10^{-4} s^{-1}$*) and high (* $k_{on} = 10^5 M^{-1} s^{-1}$ and $k_{off} = 10^{-4} s^{-1}$*) affinity interactions, respectively. The binding rate was calculated as the slope of bound target concentration vs. time curve, in a time frame of 60 min, at the bottom of the pore.*

Characterization of PSi with Different Layer Thicknesses

PSi thin films were electrochemically etched at 375 mA cm^{-2} for different time periods, to create layers with different thicknesses. The porosity and layer thickness of each nanostructure were determined by spectroscopic liquid infiltration method (SLIM), as previously described [4]. The results are presented in Table S3.

Table S3. *Etching time and characterization results by SLIM*

Etching Time (s)	Porosity (%)	Thickness (µm)
60	72±1	11.3±0.3
30	77±1	5.5±0.2
10	73±4	1.92±0.01
5	-	~0.9*

*The PSi layer fabricated by electrochemical etching for 5 s could not be analyzed by SLIM. Thus, the thickness was determined by cross section imaging with high-resolution scanning electron microscopy (HRSEM).

Figure S6 presents HRSEM (Carl Zeiss Ultra Plus, at an accelerating voltage of 1 keV) top view micrographs of the different PSi films, as well as the reflectivity spectrum, measured in air. The pore diameter and porosity are similar for the different layers; thus, the differences in the reflectivity spectrum are attributed to the different thicknesses of the films.

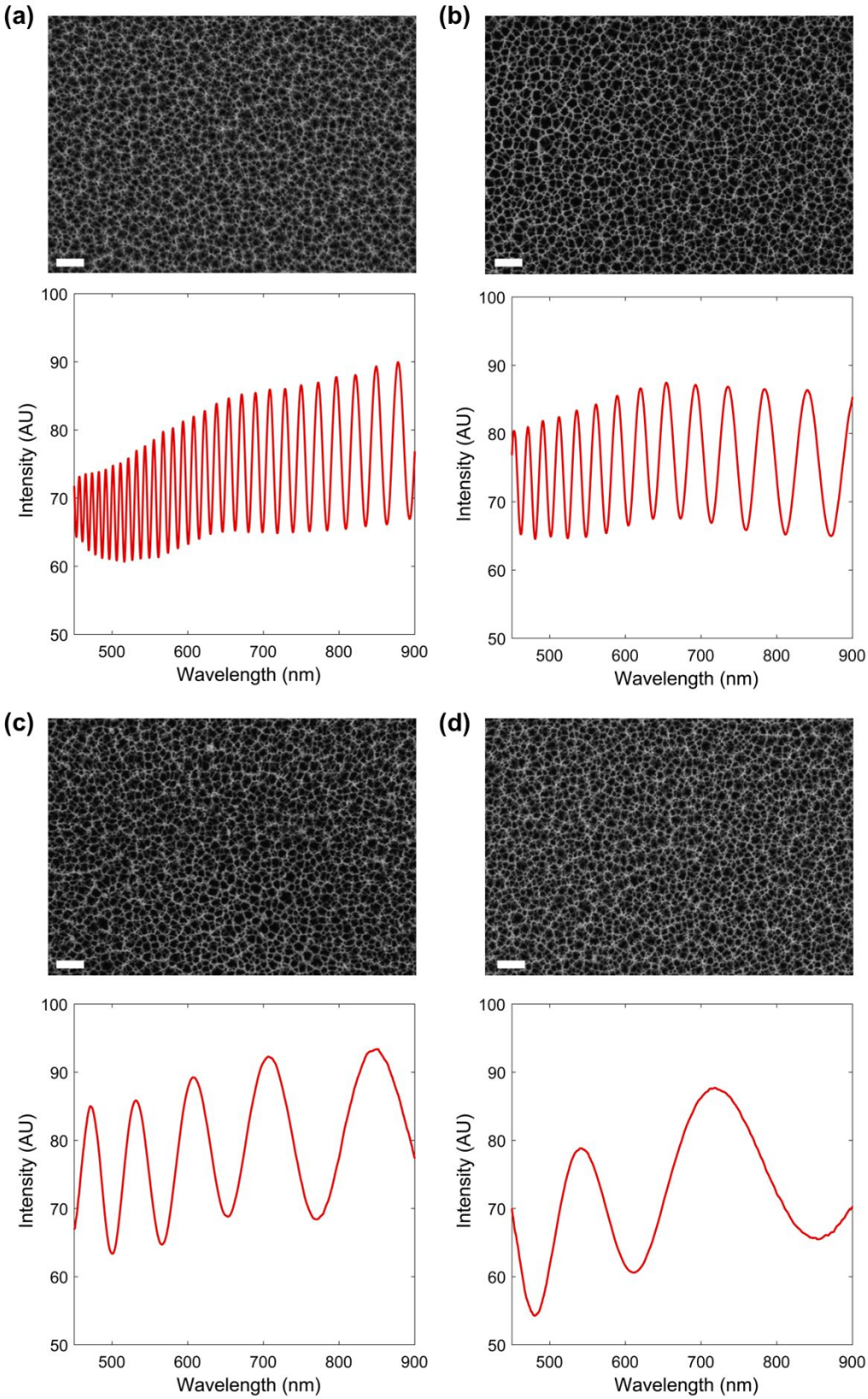

Figure S6. *Top view SEM micrographs and reflectivity spectra of PSi with different layer thicknesses: (a) 11.3±0.3 µm; (b) 5.5±0.2 µm; (c) 1.92±0.01 µm and (d) ~0.9 µm. For (a-c) the thickness was determined by SLIM analysis, while the reflectivity spectrum of structure (d) could not be reliably analyzed by FFT. Thus, the thickness of a cross section was evaluated by SEM. The scale bar is 200 nm.*

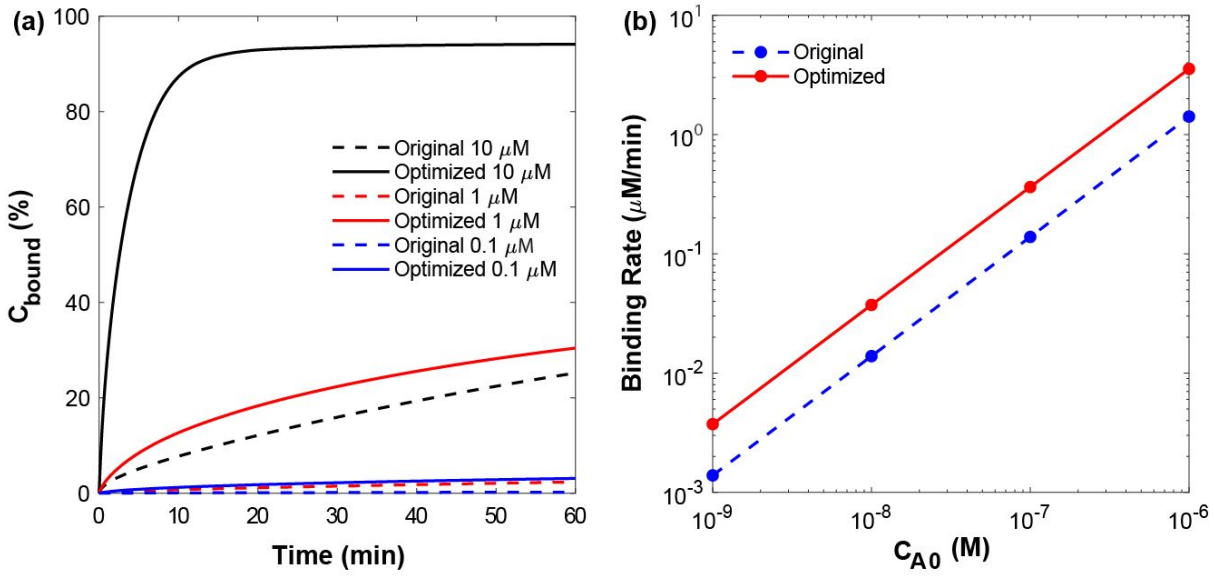

Figure S7. *(a) Simulated binding rates for the porous model for an optimized aptasensor (porous layer thickness of 2 μm and capture probe density of $2.3 \cdot 10^{-9}$ mol m^{-2}) vs. the original aptasensor (porous layer thickness of 5.5 μm and capture probe density of $1.2 \cdot 10^{-8}$ mol m^{-2}), for different target concentrations. The optimized parameters were chosen according to the numerical simulation results of the effect of the PSi thickness and capture probe density on the target binding rate. Specifically, for the thickness, this value ensures a reliable analysis of the optical signal. The curves present the bound analyte, normalized to the probe concentration, at the bottom of the pore as a function of time. (b) Comparison of the simulated binding rates for the optimized and original aptasensors as a function of target concentration. The binding rate was calculated as the slope of bound target concentration vs. time curve, in a time frame of 60 min, at the bottom of the pore. Kinetic parameters were set to* $k_{on} = 1.21 \cdot 10^{3} M^{-1} s^{-1}$ and $k_{off} = 6.32 \cdot 10^{-4} s^{-1}$.

References

1. Lazzara, T. D.; Mey, I.; Steinem, C.; Janshoff, A., Benefits and Limitations of Porous Substrates as Biosensors for Protein Adsorption. *Analytical Chemistry* **2011,** *83* (14), 5624-5630.

2. Stoltenburg, R.; Schubert, T.; Strehlitz, B., In vitro Selection and Interaction Studies of a DNA Aptamer Targeting Protein A. *PLoS One* **2015,** *10* (7), e0134403-e0134403.

3. Massad-Ivanir, N.; Friedman, T.; Nahor, A.; Eichler, S.; Bonanno, L. M.; Sa'ar, A.; Segal, E., Hydrogels synthesized in electrochemically machined porous Si hosts: effect of nano-scale confinement on polymer properties. *Soft Matter* **2012,** *8* (35), 9166-9176.

4. Sailor, M. J., *Porous silicon in practice: preparation, characterization and applications*. John Wiley & Sons: 2012.